

Balmer Decrement and IRX Break in Tracing Dust Attenuation at Scales of Individual Star-forming Regions in NGC 628

Man Qiao^{1,2}, Mingfeng Liu³, Zongfei Lyu^{1,2}, Shuang Liu^{1,2}, Chao Yang^{1,2},
Dong Dong Shi⁴, Fangxia An¹, Zhizheng Pan¹, Wenhao Liu¹, Binyang Liu¹, Run Wen^{1,2},
Yu Heng Zhang^{1,2} and Xian Zhong Zheng⁵

¹ Purple Mountain Observatory, Chinese Academy of Sciences, 10 Yuanhua Road, Nanjing
210023, China

² School of Astronomy and Space Science, University of Science and Technology of China, Hefei
230026, China

³ Department of Physics and Institute of Theoretical Physics, Nanjing Normal University,
Nanjing 210023, China

⁴ Center for Fundamental Physics, School of Mechanics and Optoelectronic Physics, Anhui
University of Science and Technology, Huainan 232001, China

⁵ Tsung-Dao Lee Institute and Key Laboratory for Particle Physics, Astrophysics and
Cosmology, Ministry of Education, Shanghai Jiao Tong University, Shanghai 201210, China;
xzzheng@sjtu.edu.cn

Received 20xx month day; accepted 20xx month day

Abstract We investigate the relationships between infrared excess ($\text{IRX} = L_{\text{IR}}/L_{\text{UV}}$) and Balmer decrement ($\text{H}\alpha/\text{H}\beta$) as indicators of dust attenuation for 609 H II regions at scales of $\sim 50\text{--}200$ pc in NGC 628, utilizing data from AstroSat, James Webb Space Telescope (JWST) and Multi Unit Spectroscopic Explorer (MUSE). Our findings indicate that about three fifths of the sample H II regions reside within the regime occupied by local star-forming galaxies (SFGs) along the dust attenuation correlation described by their corresponding color excess parameters $E(B - V)_{\text{IRX}} = 0.51 E(B - V)_{\text{H}\alpha/\text{H}\beta}$. Nearly 27% of the sample exhibits $E(B - V)_{\text{IRX}} > E(B - V)_{\text{H}\alpha/\text{H}\beta}$, while a small fraction ($\sim 13\%$) displays significantly lower $E(B - V)_{\text{IRX}}$ compared to $E(B - V)_{\text{H}\alpha/\text{H}\beta}$. These results suggest that the correlation between the two dust attenuation indicators no longer holds for spatially resolved H II regions. Furthermore, the ratio of $E(B - V)_{\text{IRX}}$ to $E(B - V)_{\text{H}\alpha/\text{H}\beta}$ remains unaffected by various physical parameters of the H II regions, including star formation rate (SFR), SFR surface density, infrared

luminosity (L_{IR}), L_{IR} surface density, stellar mass, gas-phase metallicity, circularized radius, and the distance to galactic center. We argue that the ratio is primarily influenced by the evolution of surrounding interstellar medium (ISM) of the star-forming regions, transitioning from an early dense and thick phase to the late blown-away stage.

Key words: dust: extinction — galaxies: ISM — galaxies: individual — galaxies: star formation

1 INTRODUCTION

The interplay between stars, gas, metals and dust within galaxies involves complex processes that govern star formation history, chemical enrichment and structural growth. These interactions ultimately influence the appearance of galaxies and their spectral energy distribution (SED). Among these processes, dust attenuation plays a crucial role in reshaping observable characteristics of galaxies (Draine 2003; Galliano et al. 2018; Salim & Narayanan 2020). Although dust comprises only a small fraction ($\sim 1\%$) of the interstellar medium (ISM) in star-forming galaxies (SFGs), but the thermal radiation emitted in the far-infrared — resulting from dust absorbing the ultraviolet (UV) and optical radiation primarily from young stars — accounts for nearly half of the total energy budget of the extragalactic radiation background (e.g. Dole et al. 2006). Therefore, a better understanding of dust attenuation is essential for accurate measurements of galaxy observables (Kennicutt 1998; Calzetti et al. 2000; Buat et al. 2005) and for a comprehensive understanding of the cosmic baryon cycle (Péroux & Howk 2020).

Galaxy dust attenuation quantifies the fraction of light that is diminished by dust through absorption and net scattering (both away from and back into the line of sight), as well as the effects arising from the star-dust geometry (Salim & Narayanan 2020). In practice, the slope of the ultraviolet (UV) continuum (1216 – 3000Å, noted as β), the Balmer decrement ($H\alpha/H\beta$), and the infrared excess (IRX: the ratio of infrared to UV luminosity) are commonly used as indicators of dust attenuation. Balmer lines originate from H II regions, which typically have lifetimes of approximately 10^7 years and are often surrounded by dense molecular clouds located in the inner disk component of a galaxy (Kennicutt & Evans 2012). Therefore, the Balmer decrement records a stronger dust attenuation compared to the average across the entire galaxy. The infrared excess (IRX) associates the infrared (IR) emission with the UV and optical radiation absorbed and re-emitted by dust, making it a good proxy for the average dust column density in SFGs where UV-emitting stars and dust are homogeneously mixed (Qin et al. 2024). IRX accounts for the global dust attenuation not only in the H II regions but also in the diffuse ISM. The UV slope β reflects the reddening of the intrinsic stellar UV continuum, influenced by dust opacity, the dust attenuation curve, and the intrinsic slope (Qin et al. 2022).

The relationships among IRX, $H\alpha/H\beta$, and β have been extensively examined in the literature. However, the results have often been controversial. The IRX– β relation demonstrates a positive

correlation between the two indicators (Meurer et al. 1995, 1999; Liang et al. 2021; Duffy et al. 2023; Hamed et al. 2023), but the scatter around this correlation is suggested to be driven by variations in the slope of the dust attenuation curve, the ratio of the present to past averaged star formation rate (SFR) (Kong et al. 2004; Burgarella et al. 2005), and the star-dust geometry (Wang et al. 2018). In comparison to IRX, $H\alpha/H\beta$ tends to overestimate overall dust attenuation in galaxies. This has led to a ratio of $E(B - V)$ (color excess, defined as the attenuation in the B -band minus that of in the V -band) between IRX and $H\alpha/H\beta$ being reported as 0.44 in some studies (Calzetti 2001; Wuyts et al. 2013), in contrast to a median value of 0.51 for the ratio that varies with the specific SFR surface density (Qin et al. 2019b). Given that IRX is found to be jointly determined by SFR, galaxy size (R_e), axial ratio (b/a) and metallicity but stellar mass (M_*), following a universal IRX scaling relation (Qin et al. 2019a; Qiao et al. 2024; Qin et al. 2024), the correlations between one dust attenuation indicator and other galaxy parameters (e.g. $H\alpha/H\beta$ versus M_* ; Zahid et al. 2017) are likely affected by their dependence on these four parameters (i.e., SFR, R_e , b/a and metallicity), and may thus manifest as indirect and non-causal correlations. Furthermore, previous studies have mostly treated galaxies as unresolved systems, examining the correlations between dust attenuation indicators in a statistical manner. A spatially resolved investigation into how radiation from newly-formed stars is attenuated by the surrounding dust in both the dense and diffuse ISM components, as well as how contributions from different components contribute to overall attenuation, will provide insights into reconciling the differing results.

With high-resolution imaging observations in the optical with the *Hubble Space Telescope* (HST) and in the near-IR and middle-IR with the *James Webb Space Telescope* (JWST), the stellar and dust emission in nearby galaxies can be spatially resolved down to the scales of individual H II regions. Kruijssen et al. (2019) unraveled that in nearby SFGs Balmer line emission from the H II regions and CO emission from molecular clouds no longer trace each other at spatial scales of $<\sim 100$ pc. In this work, we utilize the high-resolution multi-wavelength data of NGC 628 (i.e. M74) to carry out a spatially resolved study of IRX and $H\alpha/H\beta$ to scales of H II regions, aimed at investigating the differences between the two in tracing dust attenuation.

This paper is organized as follows: In Section 2, we present a brief description of the data. Section 3 provides data reduction and analysis. Our results are shown in Section 4. We discuss our results in Section 5 and give a summary in Section 6. A standard Λ CDM cosmology with $H_0 = 70 \text{ km}^{-1} \text{ Mpc}^{-1}$, $\Omega_\Lambda = 0.7$ and $\Omega_m = 0.3$, and a Chabrier (2003) Initial Mass Function (IMF) are adopted throughout the paper.

2 DATA

NGC 628 is a star-forming spiral galaxy nearly face-on and its basic parameters are given in Table 1. NGC 628 has been extensively observed and multi-band high-resolution imaging and spectroscopic data are publicly available. We make use of spectroscopic data from the Physics at High Angular resolution in Nearby GalaxieS (PHANGS)-Multi Unit Spectroscopic Explorer (MUSE) survey

Table 1: Basic Parameters of NGC 628.

Parameter	Value	Reference
R.A. (J2000)	01 ^h 36 ^m 41. ^s 747	NASA/IPAC Extragalactic Database (NED)
Dec. (J2000)	+15 ^d 47 ^m 01. ^s 18	NASA/IPAC Extragalactic Database (NED)
Distance	9.84 Mpc	Anand et al. (2021)
Stellar Mass	10 ^{10.24} M _⊙	Leroy et al. (2021)
Star Formation Rate	1.73 M _⊙ yr ⁻¹	Leroy et al. (2021)
Inclination	8.9°	Lang et al. (2020)
Position Angle	20.7°	Leroy et al. (2021)
Morphological Type	SA(s)c	Buta et al. (2015)

(Emsellem et al. 2022), the IR data from the PHANGS-James Webb Space Telescope (JWST) survey (project-ID 02107; Lee et al. 2023), and the UV data from the PHANGS-AstroSat survey (Hassani et al. 2024).

2.1 PHANGS-MUSE

PHANGS-MUSE made use of the MUSE integral field spectrograph on board the Very Large Telescope (VLT) at European Southern Observatory (ESO) mapping 19 massive ($9.4 < \log M_*/M_\odot < 11.0$) nearby ($D \lesssim 20$ Mpc) star-forming disk galaxies (Emsellem et al. 2022). The science-ready data cubes and data products are available ¹ (DR1.0). Congiu et al. (2023) presented a catalogue of ionized nebulae distributed across the 19 galaxies of the PHANGS-MUSE sample, using a new model-comparison-based algorithm that exploited the principle of the odds ratio to assign a probabilistic classification to each nebula. The catalogue contains spectral and spatial information for over 40 000 ionized nebulae. In our study, we utilize this ionized nebula catalogue to select H II regions within NGC 628, providing positions, radius, H α flux and H β flux of each of the selected H II regions of our sample (see Section 3.3 for more details).

2.2 PHANGS-JWST

PHANGS-JWST is a JWST Cycle 1 treasury program to image 19 nearby ($D < 20$ Mpc) main-sequence spiral galaxies at spatial scales of $\sim 5 - 50$ pc in eight JWST filters from 2 to 21 μ m using the Near Infrared Camera (NIRCam) through filters F200W, F300M, F335M, and F360M, and the Mid-InfraRed Instrument (MIRI) through filters F770W, F1000W, F1130W, and F2100W (Lee et al. 2023; Williams et al. 2024). The unprecedented sensitivity and angular resolution of JWST enable us to map infrared emission from the young stellar populations and dusty ISM across the entire disks of sample galaxies. Williams et al. (2024) presented a full public data release² (DR1.0.1) from the PHANGS-JWST Cycle 1 treasury program. NGC 628 is one of the 19 galaxies, with JWST eight-band imaging observations covering the central region of $3'.8 \times 2'.2$ (11 kpc \times 6.3 kpc) (Watkins et al. 2023). The pixel scales of these images are $0''.03$ (F200W), $0''.06$ (F300M, F335M, F360M),

¹ <https://www.canfar.net/storage/vault/list/phangs/RELEASES/PHANGS-MUSE>

² <https://archive.stsci.edu/hlsp/phangs/phangs-jwst>

0'11 (F770W, F1000W, F1130W, F2100W). We use these imaging data of NGC 628 to derive IR luminosity (L_{IR}) of the selected H II regions in our sample.

2.3 PHANGS-AstroSat

PHANGS-AstroSat contains multi-band UV imaging of 31 massive nearby ($D < 22$ Mpc) spiral galaxies observed with the Ultraviolet Imaging Telescope (UVIT; Kumar et al. 2012; Tandon et al. 2017) on the AstroSat satellite (Singh et al. 2014) in the wavelength range of 1480–2790 Å (Hassani et al. 2024). The adopted UV filters include one narrowband filter (N279N), three broadband filters (F148W, F154W, and N242W), and five medium-band filters (F169M, F172M, N219M, N245M, and N263M). These UV images have a pixel scale is 0'4176 and the median angular resolution of 1'4 (corresponding to a physical scale between 25 and 160 pc). We use the background-subtracted, foreground-corrected images of NGC 628 from CANFAR³, and calculate the UV luminosity (L_{UV}) for each of the H II regions in our sample.

3 DATA REDUCTION AND ANALYSIS

The UV, optical and IR science images of NGC 628 are obtained with different observing facilities and have distinct Point Spread Functions (PSF). We derive the corresponding PSF for each band image and perform image convolution to match all images to the same PSF. The same aperture is applied to all PSF-matched images in order to derive the multi-band photometry for given targets.

3.1 PSF Construction

We extract empirical PSF using point sources in each of the AstroSat/UVIT science images. Firstly, we identify the point sources in the background-subtracted and foreground-corrected images of NGC 628 by crossmatching the detected objects with the star catalog from Gaia Data Release 3 (DR3; Gaia Collaboration et al. 2023), and co-add the UV images of these stars to obtain a stacked star image. Secondly, we fit a two dimensional Moffat PSF model (Moffat 1969) to the stacked star image, and adopt the best-fitting model to be the empirical PSF for the given-band UV image. This best-fitting PSF is characterized by a compact core and extended wings (Leahy et al. 2020; Hassani et al. 2024). Doing so, we obtained empirical PSFs for all UV science images, giving the full-width at half maximum (FWHM) to be 1'393, 1'522, 1'218, 1'451, 1'644, 1'212, 1'104, 1'015, and 1'017 for PSFs in F148W, F154W, F169M, F172M, N219M, N242W, N245M, N263M, and N279N, respectively.

The actual JWST NIRCcam and MIRI science images of NGC 628 are fully filled by the target galaxy and it is hard to find a sample of isolated stars for constructing the empirical PSFs (Hoyer et al. 2023). We use the software tool WebbPSF⁴ (Perrin et al. 2012, 2014) to generate PSFs for given JWST images. Moreover, JWST's PSF varies in both the spatial and temporal dimensions.

³ <https://www.canfar.net/storage/vault/list/phangs/RELEASES/PHANGS-AstroSat>

⁴ <https://webbpsf.readthedocs.io/en/stable/index.html>

WebbPSF is suggested to be a better way to precisely generate PSFs for the JWST NIRCcam and MIRI images (Nardiello et al. 2022).

3.2 PSF Matching

We aim to derive dust attenuation from the UV and IR fluxes of spatially resolved H II regions within NGC 628. It is necessary to match all images to the same PSF. This can be done by resampling high-resolution images to have the same pixel scale as the image of the lowest resolution and then convolve the resampled image with corresponding convolution kernels. Among the science images of all bands that we use, the UV images from AstroSat/UVIT have the lowest resolution, and UVIT-N219M image has the largest PSF FWHM. We thus resample JWST images to have the same pixel scale ($0''.4176$) and area coverage as the AstroSat/UVIT images. Then, JWST and AstroSat/UVIT PSFs are used to generate convolution kernels using the convolution kernels generated via the Python-based PSF Homogenization kERnels (PyPHER)⁵ (Boucaud et al. 2016). The kernels are used to convolve the corresponding eight resampled JWST and eight UVIT images, and obtained the PSF-matched JWST and UVIT images to the AstroSat/UVIT-N219M images.

Additionally, to create the RGB image of NGC 628, we extract the H α map of NGC 628 from the MUSE data cubes, and resample the MUSE H α map to the same pixel scale as the AstroSat UVIT images ($0''.4176$). Figure 1 presents the RGB image of NGC 628, where the red, green and blue channels correspond to the JWST/MIRI F2100W image, MUSE H α map and AstroSat/UVIT F148W image, respectively.

3.3 Selection for H II Regions

Our sample of H II regions of NGC 628 are selected from the ionized nebula catalogue given by Congiu et al. (2023). In total 40 920 nebulae are detected in 19 nearby galaxies observed by the PHANGS-MUSE survey. These nebulae are identified from a channel-integrated flux image of [O III] λ 5007, H α and [S II] λ λ 6717,6731 lines, and classified into three types: H II regions, planetary nebulae and supernova remnants. In total 2 798 H II regions are identified in NGC 628. By limiting the H II regions in the overlap area of the MUSE, JWST, and AstroSat observations (Emsellem et al. 2022; Lee et al. 2023; Hassani et al. 2024), we obtain a sample of 1 921 H II regions in NGC 628 with the MUSE, JWST and AstroSat observations after removing those at the edges of the JWST and AstroSat images. We use this sample of 1 921 H II regions for our further analyses.

3.4 Aperture Photometry

We notice that H II regions are located within the complex spiral structures of NGC 628, making the photometric measurement of their UV and IR fluxes challenging. To reduce contamination from surrounding diffuse emissions, we employ a circular annulus to estimate the local background, facilitating subtraction in aperture photometry of the targets. We use the software tool PHOTUTILS (Bradley et al. 2024) to determine the local background and perform aperture photometry in the

⁵ <https://pypher.readthedocs.io/en/latest/>

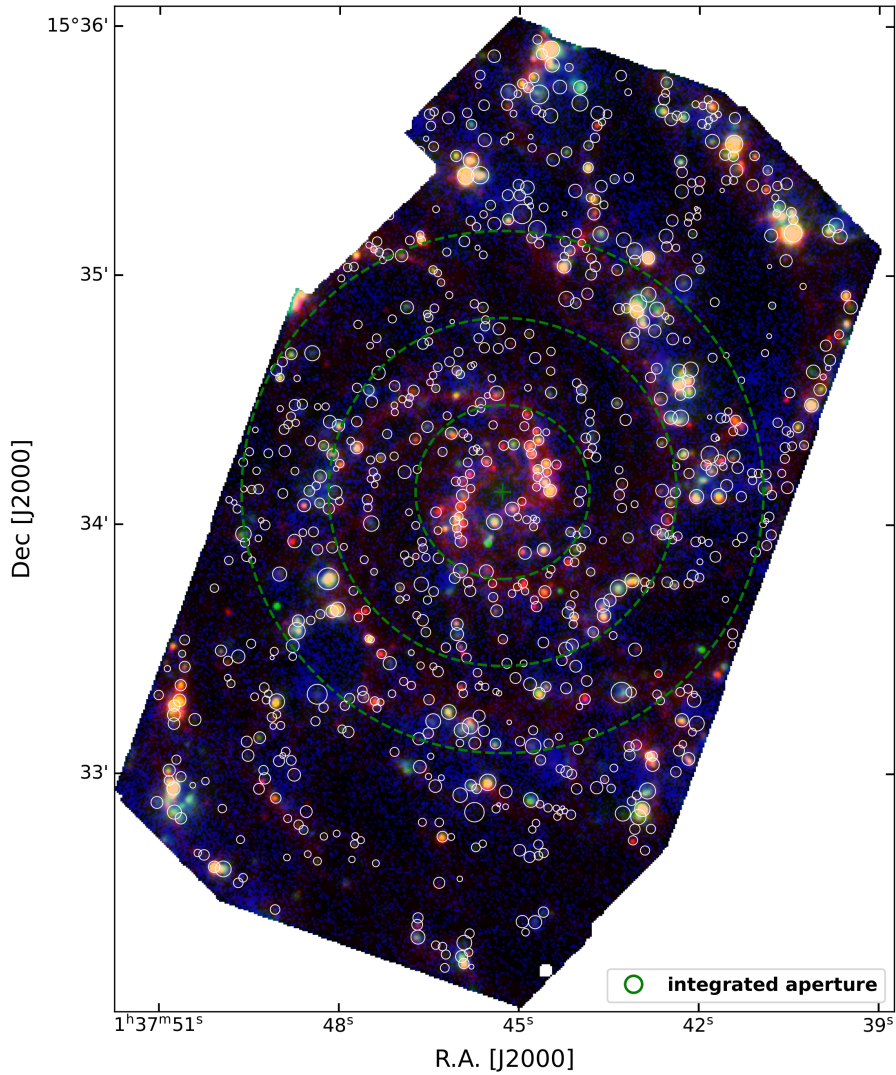


Fig. 1: Distribution of 609 H II regions for NGC 628. The white solid circles represent the photometric apertures of the final 609 H II regions of NGC 628 in our sample with circularized radius, and the background refers to the RGB image of NGC 628 obtained by combining the JWST MIRI F2100W infrared image (red), the MUSE $H\alpha$ map (green), and AstroSat UVIT N148W ultraviolet image (blue). The green dashed circles demonstrate the three apertures we used to analyze the integrated dust attenuation, with radii of 1.0, 2.0, and 3.0 kpc.

PSF-matched images from the AstroSat and JWST observations for the selected H II regions. The released JWST image sets include science and error images, while Astrosat image sets only provide science images. We thus perform aperture photometry with errors derived from the error maps for JWST, and as 5 percent for AstroSat following Hassani et al. (2024). When estimating the local background for each H II region, we first mask out surrounding H II regions to mitigate their contamination. We then calculate the local background using an annulus with inner and outer radii of $1.5r$ and $2r$, where r is the circularized radius of the target H II region. By the way, we test varying annulus sizes for background estimation, and the results demonstrate that dust attenuation remains consistent. The aperture photometry with the same aperture sizes as ionized

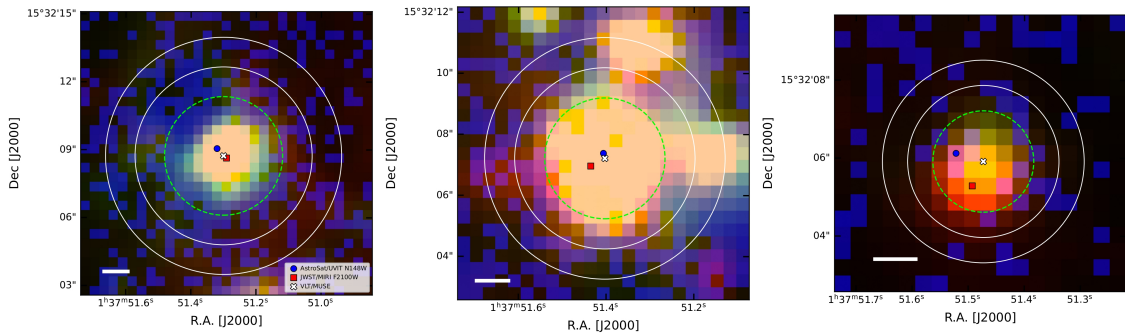


Fig. 2: Example images of the selected aperture and annulus for three H II regions of different sizes, with radii of 125 pc, 94 pc, and 62 pc. The dashed green circles represent the photometric apertures with circularized radius of H II regions from the ionized nebula catalogue, while the solid white annuli are used to estimate the local background, with inner and outer radii of $1.5r$ and $2r$, where r is the circularized radius of the target H II region. The RGB images are obtained by combining the JWST MIRI F2100W infrared image (red), the MUSE $H\alpha$ map (green), and AstroSat UVIT N148W ultraviolet image (blue). The white crosses, red squares and blue circles mark the centroid positions of H II regions in $H\alpha$, IR and UV bands. The solid white lines in lower-left corner indicates a spatial scale of 50 pc.

nebula catalogue given by Congiu et al. (2023) is performed on the UV and IR images. We provide example images of the selected aperture and annulus for three H II regions of different sizes, with radii of 125 pc, 94 pc, and 62 pc, as shown in Figure 2. The selected aperture is large enough to encompass the entire H II region, while the annulus is sufficiently distant to avoid contamination from the target.

3.5 UV and IR Luminosities, and SFR

The UV and IR luminosities of our sample H II regions are derived by fitting their SEDs composed of nine AstroSat UV bands and eight JWST NIR and mid-IR bands, using the software Code Investigating GALaxy Emission (CIGALE; Boquien et al. 2019). Stellar spectral templates with Chabrier stellar IMF (Chabrier 2003) and Solar metallicity from the Bruzual & Charlot (2003, BC03) stellar population synthesis model are adopted in the fitting. The star formation history is assumed to follow a delayed form: $\text{SFR}(t) \propto t/\tau^2 e^{-t/\tau}$ for $0 \leq t \leq t_0$, where t_0 is the age of the onset of star formation, and τ is the time at which the SFR peaks. An additional recent decline starburst is also adopted, with the stellar age varying from 10 to 200 Myr, and the e-folding time varying from 100 to 150 Myr. The Calzetti attenuation law (Calzetti et al. 2000) is adopted to count the dust attenuation with $E(B - V)$ ranging from 0.1 to 0.5 mag. Figure 3 shows an example of the best-fitting model of the SED in the UV from CIGALE.

The dust emission SED templates from Draine & Li (2007) are employed in our SED fitting. We assume mass fraction of polycyclic aromatic hydrocarbon (PAH) is in the range of [0.47, 4.58], and the fraction of illumination ranges over [0, 1]. The minimum and maximum radiation field

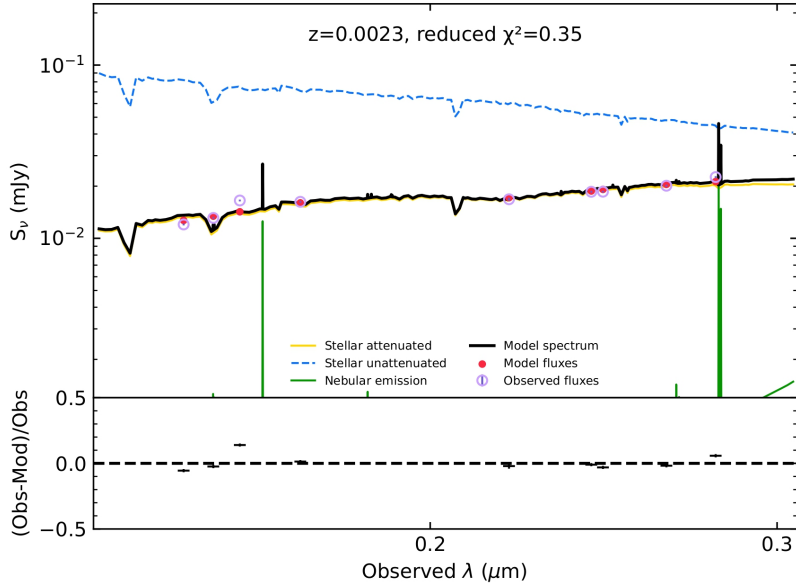


Fig. 3: An example of the best-fitting UV spectrum model from CIGALE for the SED of an H II region.

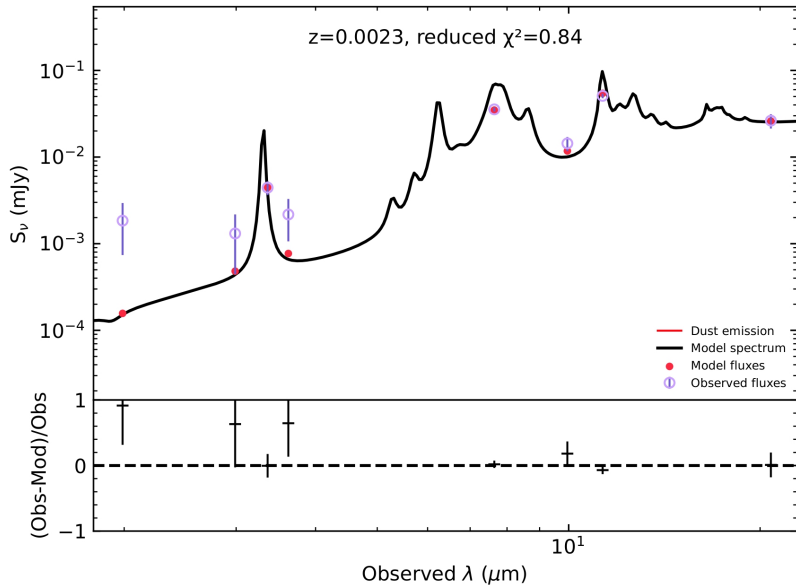


Fig. 4: An example of the best-fitting IR spectrum model from CIGALE for the SED of an H II region.

are in the range of 0.1 to 25 and 10^3 to 10^6 , respectively. Figure 4 illustrates an example of the best-fitting model to the observed dust SED.

The UV luminosity (1216–3000 Å) and the IR luminosity (8–1000 μm) are calculated from the integration of the best-fitting SED. We also calculate the $\text{SFR} = 1.09 \times 10^{-10} (L_{\text{IR}} + 2.2L_{\text{UV}})$

(Chabrier 2003; Bell et al. 2005), where L_{IR} and L_{UV} are given in units of L_{\odot} with $L_{\odot} = 3.83 \times 10^{33} \text{ erg s}^{-1}$ and SFR is given in units of $M_{\odot} \text{ yr}^{-1}$ with $M_{\odot} = 1.99 \times 10^{33} \text{ g}$.

3.6 Metallicity

The strong-line ratios ($[\text{O II}] \lambda 3727 + [\text{O III}] \lambda \lambda 4959, 5007 / \text{H}\beta$ (R23), $[\text{O III}] \lambda 5007 / [\text{O II}] \lambda 3727$ (O32), $[\text{N II}] \lambda 6584 / \text{H}\alpha$ (N2), or $([\text{O III}] \lambda 5007 / \text{H}\beta) / ([\text{N II}] \lambda 6584 / \text{H}\alpha)$ (O3N2), are the most widely used metallicity indicators (e.g. McGaugh 1991; Storchi-Bergmann et al. 1994; Kewley & Dopita 2002; Pettini & Pagel 2004; Maiolino et al. 2008; Zahid et al. 2014; Curti et al. 2017; Sanders et al. 2024). To be consistent with Qin et al. (2019b), we choose N2 to calculate the gas-phase metallicity of the H II regions in NGC 628. The oxygen abundance (O/H) is estimated following the conversion formula given by Pettini & Pagel (2004) as $12 + \log(\text{O}/\text{H}) = 0.32 \times \text{N2}^3 + 1.26 \times \text{N2}^2 + 2.03 \times \text{N2} + 9.37$, with $\text{N2} = \log([\text{N II}] \lambda 6584 / \text{H}\alpha)$. The diffuse ionized gas (DIG)-corrected fluxes of $[\text{N II}] \lambda 6584$ and $\text{H}\alpha$ of our H II regions are from the ionized nebula catalogue. Note that the valid range of N2 is $[-2.5, -0.3]$, corresponding to $12 + \log(\text{O}/\text{H})$ in the range of $[7.17, 8.86]$ (Pettini & Pagel 2004). Therefore, we exclude H II regions with N2 out of the valid range and keep the rest 1574 H II regions for our analyses.

3.7 Dust Attenuation Parameters

The IR excess parameter IRX can be directly obtained as $\text{IRX} = L_{\text{IR}}/L_{\text{UV}}$ for the 1574 H II regions in NGC 628, and $\text{H}\alpha/\text{H}\beta$ come from the ionized nebula catalogue. The two dust attenuation indicators are then converted into color excess as $E(B - V)_{\text{IRX}}$ and $E(B - V)_{\text{H}\alpha/\text{H}\beta}$, respectively. The conversion is done following

$$\begin{aligned} E(B - V)_{\text{IRX}} &= A_{\text{FUV}}/k_{\text{FUV}}, \text{ with} \\ A_{\text{FUV}} &= -0.0333X^3 + 0.3522X^2 + 1.1960X + 0.4967 \text{ and} \\ X &= \log(L_{\text{IR}}/L_{\text{FUV}}) = \log(\text{IRX}/1.38), \end{aligned} \quad (1)$$

where $k_{\text{FUV}} = 10.22$ for the adopted Calzetti attenuation curve (Calzetti et al. 2000), and the relation between A_{FUV} and IRX was given by Buat et al. (2005). The 1.38 is the conversion factor from far-UV (FUV) luminosity (L_{FUV}) to the UV luminosity, assuming a stellar population at age of 100 Myr formed through a constant SFR history. And the $E(B - V)_{\text{H}\alpha/\text{H}\beta}$ is given by

$$\begin{aligned} E(B - V)_{\text{H}\alpha/\text{H}\beta} &= A_{\text{H}\alpha}/k_{\text{H}\alpha}, \text{ with} \\ A_{\text{H}\alpha} &= \frac{-2.5k_{\text{H}\alpha}}{k_{\text{H}\beta} - k_{\text{H}\alpha}} \log\left(\frac{2.86}{\text{H}\alpha/\text{H}\beta}\right), \end{aligned} \quad (2)$$

where $k_{\text{H}\alpha} = 3.31$ and $k_{\text{H}\beta} = 4.60$ for the adopted Calzetti attenuation curve at the wavelengths of the $\text{H}\alpha$ and $\text{H}\beta$ emission lines. And the factor of 2.86 is the intrinsic $\text{H}\alpha/\text{H}\beta$ line flux ratio, under the case B recombination condition with a temperature of $T = 10^4 \text{ K}$ and an electron density of 10^2 cm^{-3} (Osterbrock & Ferland 2006). Furthermore, to quantify the color excess discrepancy between $E(B - V)_{\text{IRX}}$ and $E(B - V)_{\text{H}\alpha/\text{H}\beta}$, the IRX-to- $\text{H}\alpha/\text{H}\beta$ color excess ratio of $R_{\text{EBV}} \equiv E(B - V)_{\text{IRX}}/E(B - V)_{\text{H}\alpha/\text{H}\beta}$ is introduced as adopted in Qin et al. (2019b).

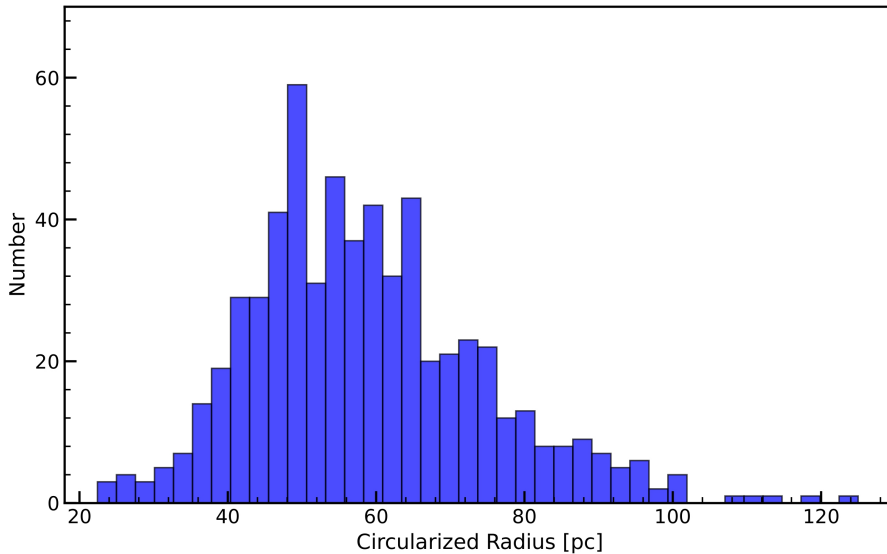


Fig. 5: Histogram of circularized radius for 609 H II regions in NGC 628.

4 RESULTS

We want to examine connections of color excess between IRX and $H\alpha/H\beta$ at scales of H II regions. Due to the photometric uncertainties, some measured fluxes are below zero. We get rid of the sample targets with negative values for fluxes of $H\alpha$ or $H\beta$ lines, UV or IR luminosities, and the estimated $E(B - V)_{H\alpha/H\beta}$ and $E(B - V)_{IRX}$. The removed objects are faint in either Balmer-line emission or in UV and IR (dust) emission. We obtain 609 data points having secure estimates of $E(B - V)_{H\alpha/H\beta}$ and $E(B - V)_{IRX}$. Figure 1 presents the distribution of these H II regions in NGC 628. The 609 H II regions exhibit sizes (circularized radius) range from 22 pc to 125 pc, and the histogram of circularized radius for these H II regions is shown in Figure 5.

Figure 6 shows comparison of $E(B - V)_{IRX}$ and $E(B - V)_{H\alpha/H\beta}$ for 609 H II regions in NGC 628. One can see that the H II regions at scales of ~ 200 pc spread much wider than local SFGs. While the local SFGs (grey-scale map) apparently form a sequence in the sense that $E(B - V)_{IRX}$ globally increases with $E(B - V)_{H\alpha/H\beta}$, the majority of the sample H II regions fall into the locus area of the local SFGs, suggesting that these H II regions are representative of these local SFGs in dust attenuation. However, some data points are located out the SFG area, e.g., these above the black dashed line or in the red box. We note that approximately 27% of the sample H II regions distribute above the one-to-one line, meaning that IRX probes a higher degree of obscuration than $H\alpha/H\beta$. Meanwhile, there is a portion of H II regions with relatively small $E(B - V)_{IRX}$ and $E(B - V)_{H\alpha/H\beta}$, which are distributed in the lower-left corner of the $E(B - V)_{IRX} - E(B - V)_{H\alpha/H\beta}$ diagram. We also calculate the integrated results of $E(B - V)_{IRX}$ and $E(B - V)_{H\alpha/H\beta}$ by selecting apertures with three different radii, including 1, 2 and 3 kpc, centered at the center of NGC 628, as well as the results from the entire observed area. We find that the relationship between the integrated $E(B - V)_{IRX}$ and $E(B - V)_{H\alpha/H\beta}$ agrees with that of the local SFGs, being near the median of $R_{EBV} = 0.51$ given by Qin et al. (2019b).

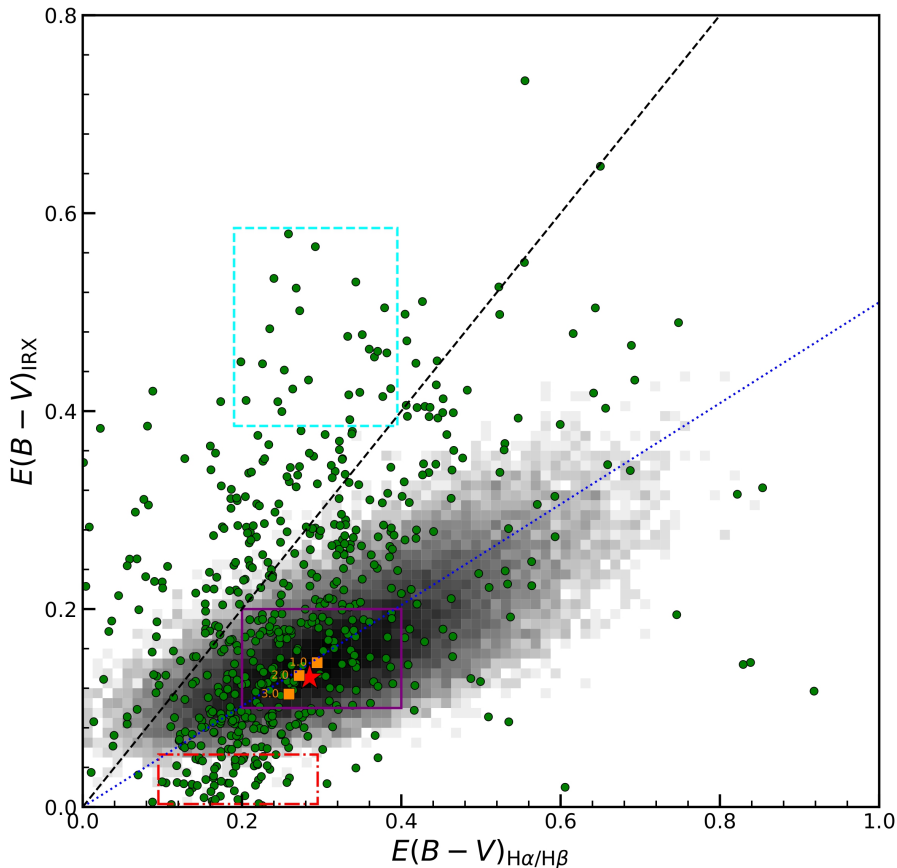


Fig. 6: Comparison of $E(B - V)_{\text{IRX}}$ and $E(B - V)_{\text{H}\alpha/\text{H}\beta}$ for 609 H II regions. The green points represent the 609 H II regions, and the background grey-scale map demonstrates the distribution of 32 354 local SFGs from Qin et al. (2019b). The black dashed line denotes the 1:1 line, and the blue dotted line shows the average ratio $E(B - V)_{\text{IRX}}/E(B - V)_{\text{H}\alpha/\text{H}\beta} = 0.51$ given in Qin et al. (2019b). The three orange squares represent the integrated $E(B - V)_{\text{IRX}}$ and $E(B - V)_{\text{H}\alpha/\text{H}\beta}$ for H II regions within the three apertures shown in Figure 1 and red star is for all H II region in our sample, respectively. And the labeled numbers denote the aperture size. The cyan (dashed), purple (solid), and red (dashed-dotted) rectangles arbitrarily mark the loci of three types of H II regions in different evolutionary stages.

We then investigate the locations of the selected H II regions in NGC 628. We selected three groups of H II regions being distinct in R_{EBV} , i.e. located separated in the $E(B - V)_{\text{IRX}} - E(B - V)_{\text{H}\alpha/\text{H}\beta}$ diagram as illustrated by the three rectangles in Figure 6. Each group represents H II regions at different evolutionary stages of star formation, and their distribution in NGC 628 is shown in Figure 7 with the same color as the rectangles in Figure 6.

The top cyan dashed rectangle in Figure 6 encloses a subsample of H II regions with $E(B - V)_{\text{IRX}} > E(B - V)_{\text{H}\alpha/\text{H}\beta}$. We can see from Figure 7 that noticeable offsets are found for these targets between their $\text{H}\alpha$ and $21 \mu\text{m}$ peaks. Figure 8 shows the histogram of central offsets between PHANGS-MUSE $\text{H}\alpha$ and PHANGS-JWST/MIRI $21 \mu\text{m}$. We suggest that these H II regions are in the early evolutionary stage of star formation, during which the newly-formed young massive stars are still largely enveloped by birth clouds. The $\text{H}\alpha$ and $\text{H}\beta$ emission from the surrounding gas

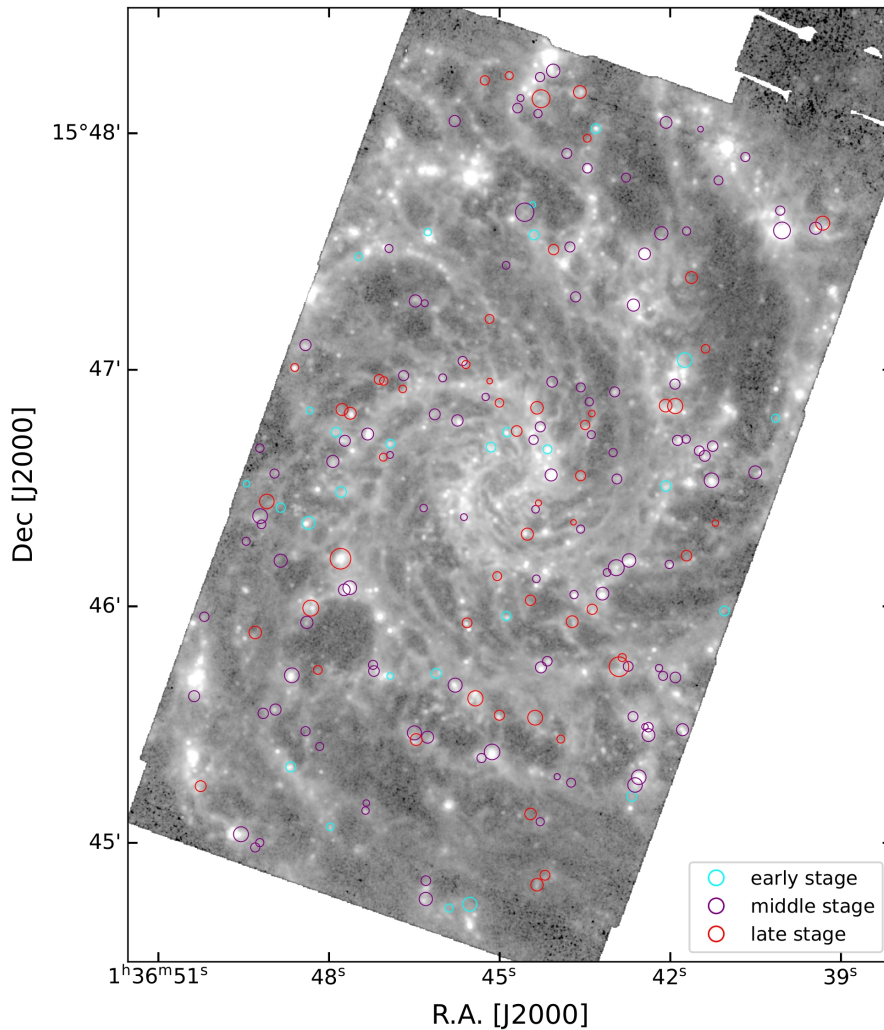


Fig. 7: Locations of three types of H II regions enclosed in the three rectangles in Figure 6. The sizes of circles are proportional to the radii of given H II regions, shown in color same as the corresponding rectangles.

ionized by the UV ionizing photons hardly penetrates the dense clouds, and only a little fraction of the UV photons can escape from some holes of the star-forming clouds, leading to relatively low $E(B - V)_{H\alpha/H\beta}$ and high $E(B - V)_{IRX}$. Chevance et al. (2020) found the typical lifetimes of molecular clouds are 10–30 Myr, and the phase without $H\alpha$ emission is about 75–90 per cent of the cloud lifetime.

On the other hand, H II regions in the middle purple solid rectangle in Figure 6 exhibit $E(B - V)_{IRX}$ and $E(B - V)_{H\alpha/H\beta}$ following the relation as observed among local SFGs, adhering to the $R_{EBV} = 0.51$ (Qin et al. 2019b). We can see from Figure 7 that the peaks of the $H\alpha$ emission from these H II regions largely overlap with the peaks at $21 \mu\text{m}$. And the central offsets of the majority of the H II regions concentrate at less than 40 pc, shown in Figure 8. We consider that these H II regions are in the middle stage of star formation, lasting 1–5 Myr (Chevance et al. 2020). During the on-going process of star formation, stellar winds drive part of the birth clouds away, allowing us to observe both Balmer line emission, and the IR and UV radiation. As a result, the

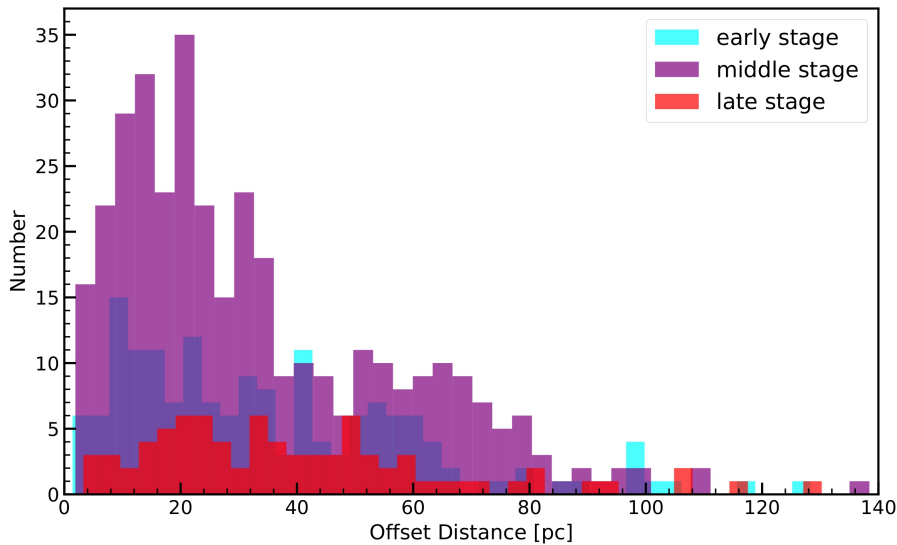


Fig. 8: The histogram of central offsets between PHANGS-MUSE $H\alpha$ and PHANGS-JWST/MIRI $21\ \mu\text{m}$ for three types of H II regions. The colors of H II regions at different evolutionary stages are the same as Figure 7.

properties exhibited by these H II regions are generally consistent with the overall dust attenuation characteristics of the local SFGs.

For the third class of H II regions as enclosed in the bottom red dashed-dotted rectangle in Figure 6, their $E(B - V)_{\text{IRX}}$ and $E(B - V)_{H\alpha/H\beta}$ are both relatively low. These H II regions are often distributed slightly away from the bridges of spiral arms of NGC 628, and most of them do not have bright $21\ \mu\text{m}$ dust emission, distinct from the first two classes of H II regions. This might indicate that these H II regions are in the late evolutionary stage of star formation, during which nearly all of the birth clouds have been blown away by stellar winds, leaving the young stars least obscured. The Balmer line emission and dust IR emission become much weaker, leading to smaller values for $E(B - V)_{\text{IRX}}$ and $E(B - V)_{H\alpha/H\beta}$.

However, the positions of these H II regions in UV (young stars) and IR (dust-reprocessed light) images may differ due to wavelength-dependent resolution, dust obscuration, or physical offsets between ionized gas and stellar/dust components. We calculate the central offsets of each H II region between PHANGS-MUSE $H\alpha$ and PHANGS-JWST/MIRI F2100W band, as well as those between PHANGS-MUSE $H\alpha$ and PHANGS-AstroSat/UVIT N148W band, as shown in Figure 9. We find that the central offsets of H II regions between different bands exhibit a random distribution, with no statistically significant correlation to the physical sizes of the H II regions.

5 DISCUSSION

We investigate the relationships between two indicators IRX ($E(B - V)_{\text{IRX}}$) and Balmer decrement ($E(B - V)_{H\alpha/H\beta}$) for 609 H II regions at scales of $\sim 50\text{--}200\ \text{pc}$ in NGC 628. We find that the relation $E(B - V)_{\text{IRX}} = 0.51 E(B - V)_{H\alpha/H\beta}$, which is established among local SFGs, does not hold for the H II regions, as illustrated in Figure 6. The scatter of data points in $E(B - V)_{\text{IRX}} - E(B - V)_{H\alpha/H\beta}$ diagram is quite large, indicating that the two indicators break in probing dust attenuation at

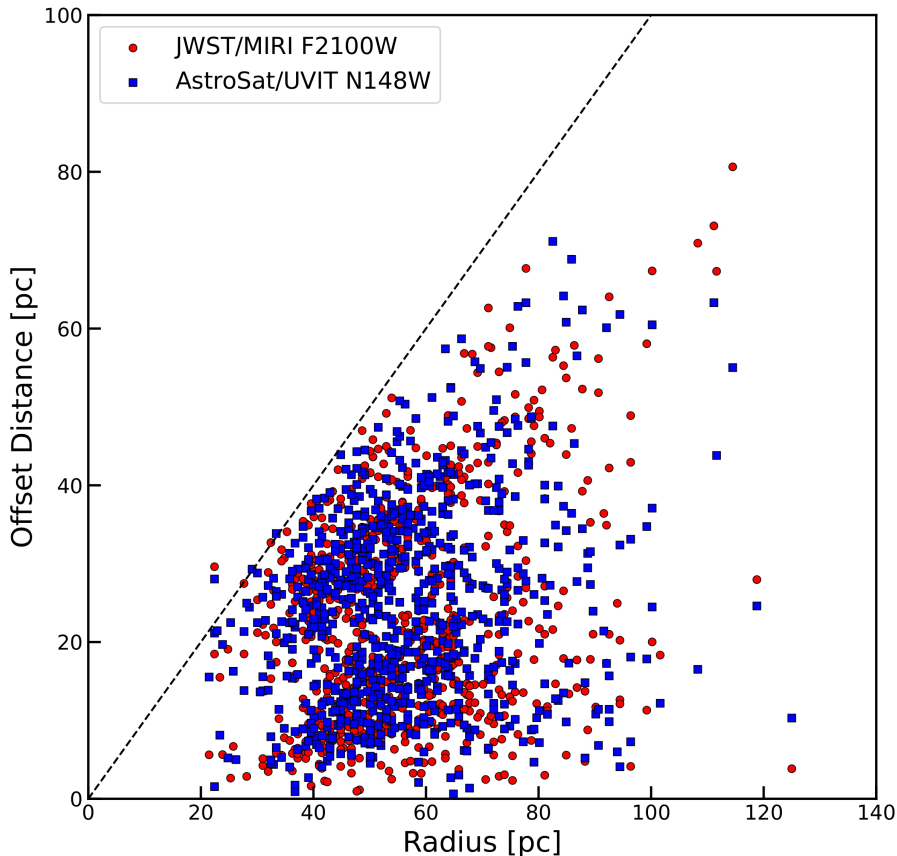


Fig. 9: The central offsets of H II regions between ionized gas and stellar/dust components. The red circles represent the central offsets between PHANGS-MUSE $H\alpha$ and PHANGS-JWST/MIRI F2100W band, while the blue squares represent those between PHANGS-MUSE $H\alpha$ and PHANGS-AstroSat/UVIT N148W band. The dashed black line marks the 1:1 line.

spatial scales of H II regions with diameters of 50 – 200 pc in NGC 628. For heavily obscured H II regions in the early evolutionary stage, IRX is a good probe for dust attenuation but $H\alpha/H\beta$ no longer works because these H II regions are optically thick. As a result, the data points of our sample H II regions do not follow a tight correlation between $E(B - V)_{\text{IRX}}$ and $E(B - V)_{H\alpha/H\beta}$. When counting dust attenuation over regions of $> \sim 0.5$ kpc scales, the integrated dust attenuation traced by IRX and $H\alpha/H\beta$ converges to the global correlation among the local SFGs. This confirms that the correlation between $E(B - V)_{\text{IRX}}$ and $E(B - V)_{H\alpha/H\beta}$ holds at scales of $> \sim 0.5$ kpc and breaks at scales of $\sim 50 - 200$ pc in NGC 628. Note that we do not attempt to determine a critical scale below which the correlation starts to deviate from the regime occupied by the local SFGs, because both the local SFGs and our sample H II regions show large spreads in size.

Interestingly, Duffy et al. (2023) found that the spatially-resolved kpc-sized star-forming regions in nearby galaxies follows nearly the same IRX- β relation as that for SFGs, indicating that the dust attenuation curve for the integrated light of galaxies remains unchanged for the kpc-scale star-forming regions (see also Ye et al. 2016). This is consistent with our results.

Furthermore, we address the connections of dust attenuation with other parameters for our 609 H II regions in NGC 628. This is done by color coding the data points in the diagram of

$E(B - V)_{\text{H}\alpha/\text{H}\beta}$ versus $E(B - V)_{\text{IRX}}$ by different physical parameters, including SFR, SFR surface density, L_{IR} , L_{IR} surface density, stellar mass, gas-phase metallicity, radius, and the distance to galactic center for each H II region. The results are shown in Figure 10. Overall, we find no apparent color pattern in the six panel, meaning that there is no statistically-significant dependence of the ratio of $E(B - V)_{\text{IRX}}$ to $E(B - V)_{\text{H}\alpha/\text{H}\beta}$ on these parameters. These results suggest that the discrepancy between IRX and $\text{H}\alpha/\text{H}\beta$ of H II regions, i.e. the location in the $E(B - V)_{\text{IRX}}$ versus $E(B - V)_{\text{H}\alpha/\text{H}\beta}$ diagram, is not controlled or influenced by these physical parameters. In contrast, the ratio exhibits a clear dependence on the sSFR surface density over galactic scales, as reported in Qin et al. (2019b). This dependence no longer holds for individual H II regions at scales of $\sim 50 - 200$ pc in NGC 628. For a galaxy, it includes not only young stars but also intermediate-age and old stars, star-forming regions, and diffuse ISM. Therefore, the overall average ratio between $E(B - V)_{\text{IRX}}$ and $E(B - V)_{\text{H}\alpha/\text{H}\beta}$ depends on the sSFR surface density. However, when focusing on individual star-forming regions, they only contain young stars and birth clouds at different evolutionary stages, possibly exhibiting distinct IRX and $\text{H}\alpha/\text{H}\beta$ from these of the entire galaxy. As a consequence, the correlation between $E(B - V)_{\text{IRX}}$ and $E(B - V)_{\text{H}\alpha/\text{H}\beta}$ breaks at scales of individual star-forming regions.

In the early stage of star formation, young massive stars remain embedded within dense natal clouds (optically thick). This leads to high $E(B - V)_{\text{IRX}}$ but low $E(B - V)_{\text{H}\alpha/\text{H}\beta}$ due to limited $\text{H}\alpha$ and $\text{H}\beta$ photons escape. In contrast, in the late stage of star formation, the surrounding dust is cleared via stellar winds (e.g. Chevance et al. 2020), leading to lower $E(B - V)_{\text{IRX}}$ and $E(B - V)_{\text{H}\alpha/\text{H}\beta}$ as IR, $\text{H}\alpha$, $\text{H}\beta$ emissions decrease. This evolutionary sequence explains the observed scatter in Figure 6. At H II region scales, the homogeneous dust-star mixture assumed in galaxy-scale studies breaks down. Clumpy dust distributions (Witt & Gordon 2000) may decouple the attenuation of UV photons (traced by IRX) from the ionized gas (traced by $\text{H}\alpha/\text{H}\beta$). Stellar winds can create cavities in the ISM, altering the relative distribution of ionized gas and dust. $\text{H}\alpha$ emission primarily traces low-density ionized gas outside dense clouds, whereas IRX remains sensitive to embedded dust within optically thick regions. This spatial decoupling could contribute to the non-linear $E(B - V)_{\text{IRX}} - E(B - V)_{\text{H}\alpha/\text{H}\beta}$ relation.

6 SUMMARY

We use the UV, NIR and MIR imaging data from PHANGS-AstroSat and PHANGS-JWST, as well as the ionized nebula catalogue derived from PHANGS-MUSE, to spatially resolve 609 H II regions in NGC 628 and examine the connections between IRX ($E(B - V)_{\text{IRX}}$) and Balmer decrement ($E(B - V)_{\text{H}\alpha/\text{H}\beta}$) in tracing dust attenuation. Our main results are summarized as follows:

1. The sample H II regions widely spread in the $E(B - V)_{\text{IRX}}$ versus $E(B - V)_{\text{H}\alpha/\text{H}\beta}$ diagram, indicating that the relation between IRX ($E(B - V)_{\text{IRX}}$) and Balmer decrement ($E(B - V)_{\text{H}\alpha/\text{H}\beta}$) (i.e., $E(B - V)_{\text{IRX}} = 0.51 E(B - V)_{\text{H}\alpha/\text{H}\beta}$) on the galaxy scale of local SFGs no longer holds for H II regions at scales of $\sim 50 - 200$ pc.

2. No dependence is found for the ratio of $E(B - V)_{\text{IRX}}$ to $E(B - V)_{\text{H}\alpha/\text{H}\beta}$ on physical parameters SFR, SFR surface density, IR luminosity, IR luminosity surface density, stellar mass, gas-phase metallicity, circularized radius, and distance to galactic center for the sample H II regions. And we find no correlations between these parameters and IRX or H α /H β .
3. We point out that the H II regions with $E(B - V)_{\text{IRX}}$ higher than $E(B - V)_{\text{H}\alpha/\text{H}\beta}$ are likely in early evolutionary stage in which the star-forming regions are heavily obscured and optically thick, while about three fifths of the regions are in the parameter range that local SFGs spread. Note that a small portion of the H II regions exhibit very small ratio of $E(B - V)_{\text{IRX}}$ to $E(B - V)_{\text{H}\alpha/\text{H}\beta}$, and we believe that these H II regions are in the late evolutionary stage in which the surrounding ISM are nearly all driven away by stellar winds.

Acknowledgements This work is supported by by the National Key Research and Development Program of China (2023YFA1608100), the National Science Foundation of China (12233005, 12073078, 12173088, 12303015), D.D.S. acknowledges the supports from Scientific Research Foundation for High-level Talents of Anhui University of Science and Technology (2024yjrc104), the National Science Foundation of Jiangsu Province (BK20231106) and the science research grants from the China Manned Space Project. X.Z.Z. is grateful to the support from STCSM through grant No. 24DX1400100.

References

- Anand, G. S., Lee, J. C., Van Dyk, S. D., et al. 2021, *MNRAS*, 501, 3621 4
- Bell, E. F., Papovich, C., Wolf, C., et al. 2005, *ApJ*, 625, 23 10
- Boquien, M., Burgarella, D., Roehlly, Y., et al. 2019, *A&A*, 622, A103 8
- Boucaud, A., Bocchio, M., Abergel, A., et al. 2016, *A&A*, 596, A63 6
- Bradley, L., Sipőcz, B., Robitaille, T., et al. 2024, *astropy/photutils: 2.0.2* 6
- Bruzual, G., & Charlot, S. 2003, *MNRAS*, 344, 1000 8
- Buat, V., Iglesias-Páramo, J., Seibert, M., et al. 2005, *ApJ*, 619, L51 2, 10
- Burgarella, D., Buat, V., & Iglesias-Páramo, J. 2005, *MNRAS*, 360, 1413 3
- Buta, R. J., Sheth, K., Athanassoula, E., et al. 2015, *ApJS*, 217, 32 4
- Calzetti, D. 2001, *PASP*, 113, 1449 3
- Calzetti, D., Armus, L., Bohlin, R. C., et al. 2000, *ApJ*, 533, 682 2, 8, 10
- Chabrier, G. 2003, *PASP*, 115, 763 3, 8, 10
- Chevance, M., Kruijssen, J. M. D., Hygate, A. P. S., et al. 2020, *MNRAS*, 493, 2872 13, 16
- Congiu, E., Blanc, G. A., Belfiore, F., et al. 2023, *A&A*, 672, A148 4, 6, 8
- Curti, M., Cresci, G., Mannucci, F., et al. 2017, *MNRAS*, 465, 1384 10
- Dole, H., Lagache, G., Puget, J. L., et al. 2006, *A&A*, 451, 417 2
- Draine, B. T. 2003, *ARA&A*, 41, 241 2
- Draine, B. T., & Li, A. 2007, *ApJ*, 657, 810 8
- Duffy, L., Molina, M., Eracleous, M., et al. 2023, *MNRAS*, 526, 904 3, 15
- Emsellem, E., Schinnerer, E., Santoro, F., et al. 2022, *A&A*, 659, A191 4, 6

- Gaia Collaboration, Vallenari, A., Brown, A. G. A., et al. 2023, *A&A*, 674, A1 5
- Galliano, F., Galametz, M., & Jones, A. P. 2018, *ARA&A*, 56, 673 2
- Hamed, M., Pistis, F., Figueira, M., et al. 2023, *A&A*, 679, A26 3
- Hassani, H., Rosolowsky, E., Koch, E. W., et al. 2024, *ApJS*, 271, 2 4, 5, 6, 7
- Hoyer, N., Pinna, F., Kamlah, A. W. H., et al. 2023, *ApJ*, 944, L25 5
- Kennicutt, R. C., & Evans, N. J. 2012, *ARA&A*, 50, 531 2
- Kennicutt, Jr., R. C. 1998, *ApJ*, 498, 541 2
- Kewley, L. J., & Dopita, M. A. 2002, *ApJS*, 142, 35 10
- Kong, X., Charlot, S., Brinchmann, J., & Fall, S. M. 2004, *MNRAS*, 349, 769 3
- Kruijssen, J. M. D., Schrubba, A., Chevance, M., et al. 2019, *Nature*, 569, 519 3
- Kumar, A., Ghosh, S. K., Hutchings, J., et al. 2012, in *Society of Photo-Optical Instrumentation Engineers (SPIE) Conference Series*, Vol. 8443, *Space Telescopes and Instrumentation 2012: Ultraviolet to Gamma Ray*, ed. T. Takahashi, S. S. Murray, & J.-W. A. den Herder, 84431N 5
- Lang, P., Meidt, S. E., Rosolowsky, E., et al. 2020, *ApJ*, 897, 122 4
- Leahy, D. A., Postma, J., Chen, Y., & Buick, M. 2020, *ApJS*, 247, 47 5
- Lee, J. C., Sandstrom, K. M., Leroy, A. K., et al. 2023, *ApJ*, 944, L17 4, 6
- Leroy, A. K., Schinnerer, E., Hughes, A., et al. 2021, *ApJS*, 257, 43 4
- Liang, L., Feldmann, R., Hayward, C. C., et al. 2021, *MNRAS*, 502, 3210 3
- Maiolino, R., Nagao, T., Grazian, A., et al. 2008, *A&A*, 488, 463 10
- McGaugh, S. S. 1991, *ApJ*, 380, 140 10
- Meurer, G. R., Heckman, T. M., & Calzetti, D. 1999, *ApJ*, 521, 64 3
- Meurer, G. R., Heckman, T. M., Leitherer, C., et al. 1995, *AJ*, 110, 2665 3
- Moffat, A. F. J. 1969, *A&A*, 3, 455 5
- Nardiello, D., Bedin, L. R., Burgasser, A., et al. 2022, *MNRAS*, 517, 484 6
- Osterbrock, D. E., & Ferland, G. J. 2006, *Astrophysics of gaseous nebulae and active galactic nuclei* 10
- Péroux, C., & Howk, J. C. 2020, *ARA&A*, 58, 363 2
- Perrin, M. D., Sivaramakrishnan, A., Lajoie, C.-P., et al. 2014, in *Society of Photo-Optical Instrumentation Engineers (SPIE) Conference Series*, Vol. 9143, *Space Telescopes and Instrumentation 2014: Optical, Infrared, and Millimeter Wave*, ed. J. M. Oschmann, Jr., M. Clampin, G. G. Fazio, & H. A. MacEwen, 91433X 5
- Perrin, M. D., Soummer, R., Elliott, E. M., Lallo, M. D., & Sivaramakrishnan, A. 2012, in *Society of Photo-Optical Instrumentation Engineers (SPIE) Conference Series*, Vol. 8442, *Space Telescopes and Instrumentation 2012: Optical, Infrared, and Millimeter Wave*, ed. M. C. Clampin, G. G. Fazio, H. A. MacEwen, & J. M. Oschmann, Jr., 84423D 5
- Pettini, M., & Pagel, B. E. J. 2004, *MNRAS*, 348, L59 10
- Qiao, M., Zheng, X. Z., Katsianis, A., et al. 2024, *MNRAS*, 528, 997 3
- Qin, J., Zheng, X. Z., Wuyts, S., Pan, Z., & Ren, J. 2019a, *MNRAS*, 485, 5733 3
- Qin, J., Zheng, X. Z., Wuyts, S., Pan, Z., & Ren, J. 2019b, *ApJ*, 886, 28 3, 10, 11, 12, 13, 16

- Qin, J., Zheng, X. Z., Fang, M., et al. 2022, MNRAS, 511, 765 2
- Qin, J., Zheng, X. Z., Wuyts, S., et al. 2024, MNRAS, 528, 658 2, 3
- Salim, S., & Narayanan, D. 2020, ARA&A, 58, 529 2
- Sanders, R. L., Shapley, A. E., Topping, M. W., Reddy, N. A., & Brammer, G. B. 2024, ApJ, 962, 24 10
- Singh, K. P., Tandon, S. N., Agrawal, P. C., et al. 2014, in Society of Photo-Optical Instrumentation Engineers (SPIE) Conference Series, Vol. 9144, Space Telescopes and Instrumentation 2014: Ultraviolet to Gamma Ray, ed. T. Takahashi, J.-W. A. den Herder, & M. Bautz, 91441S 5
- Storchi-Bergmann, T., Calzetti, D., & Kinney, A. L. 1994, ApJ, 429, 572 10
- Tandon, S. N., Subramaniam, A., Girish, V., et al. 2017, AJ, 154, 128 5
- Wang, W., Kassin, S. A., Pacifici, C., et al. 2018, ApJ, 869, 161 3
- Watkins, E. J., Barnes, A. T., Henny, K., et al. 2023, ApJ, 944, L24 4
- Williams, T. G., Lee, J. C., Larson, K. L., et al. 2024, ApJS, 273, 13 4
- Witt, A. N., & Gordon, K. D. 2000, ApJ, 528, 799 16
- Wuyts, S., Förster Schreiber, N. M., Nelson, E. J., et al. 2013, ApJ, 779, 135 3
- Ye, C., Zou, H., Lin, L., et al. 2016, ApJ, 826, 209 15
- Zahid, H. J., Dima, G. I., Kudritzki, R.-P., et al. 2014, ApJ, 791, 130 10
- Zahid, H. J., Kudritzki, R.-P., Conroy, C., Andrews, B., & Ho, I. T. 2017, ApJ, 847, 18 3

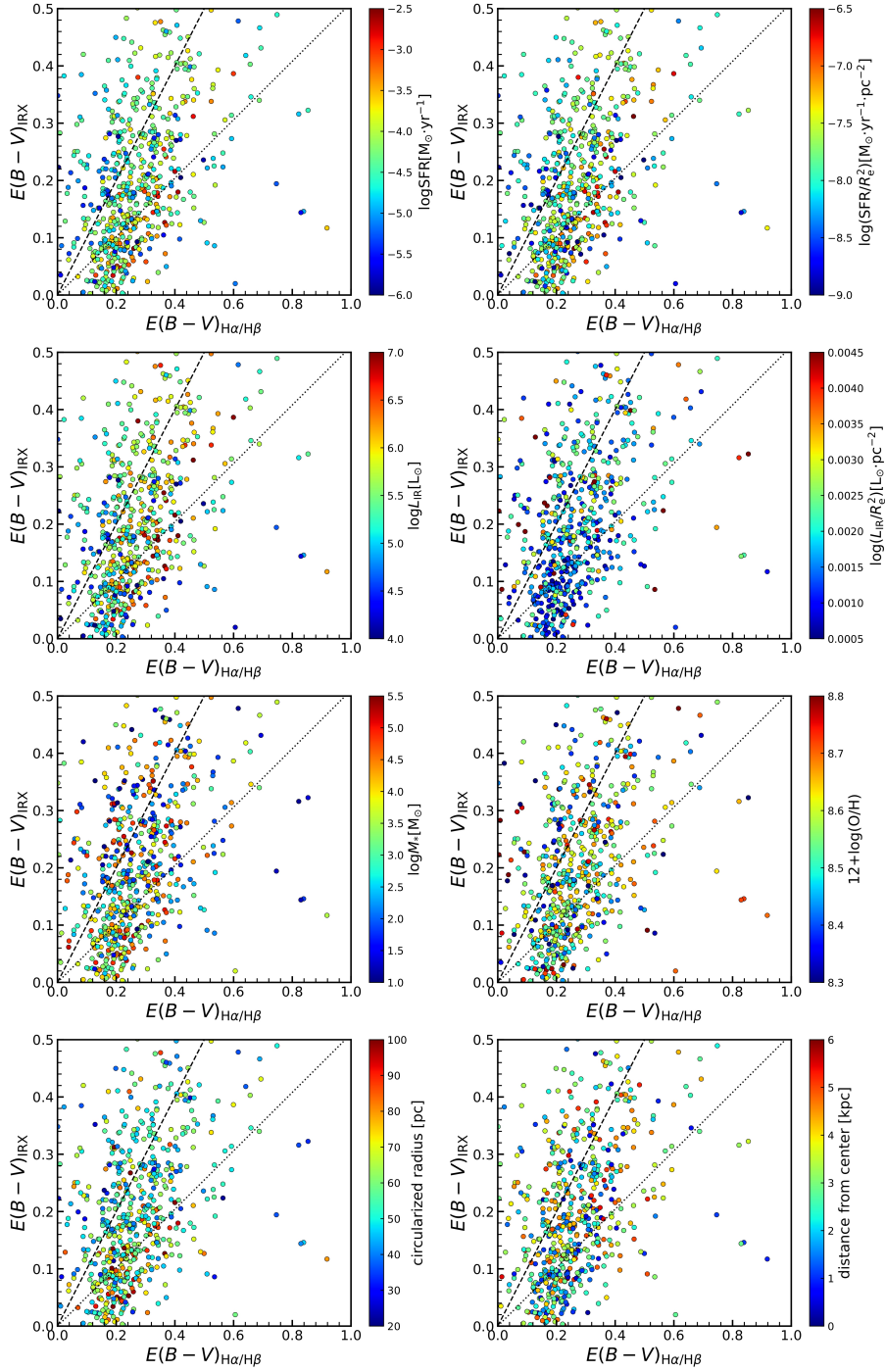


Fig. 10: Comparison between $E(B - V)_{\text{IRX}}$ and $E(B - V)_{\text{H}\alpha/\text{H}\beta}$ for a sample of 609 H II regions in NGC 628. In these panels, from left to right and top to bottom, the parameters used for color coding are SFR, SFR surface density, L_{IR} , L_{IR} surface density, stellar mass, gas-phase metallicity, radius, and the distance to galactic center, respectively. The dashed and dotted lines mark the relation of $E(B - V)_{\text{IRX}} = E(B - V)_{\text{H}\alpha/\text{H}\beta}$ (i.e., $R_{\text{EBV}} = 1$) and $E(B - V)_{\text{IRX}} = 0.51 \times E(B - V)_{\text{H}\alpha/\text{H}\beta}$ (i.e., $R_{\text{EBV}} = 0.51$).